



AIAA 95-2924

**Spatial and Temporal Distribution of Ion
Engine Accelerator Grid Erosion**

**J.E. Polk, J.R. Brophy and J. Wang
Jet Propulsion Laboratory
Pasadena CA 91109-8099**

**31st AIAA/ASME/SAE/ASEE
Joint Propulsion Conference and Exhibit
July 10-12, 1995 | San Diego, CA**

Spatial and Temporal Distribution of Ion Engine Accelerator Grid Erosion

J. E. Polk*, J. R. Brophy† and J. Wang‡
Jet Propulsion Laboratory
California Institute of Technology
Pasadena, California

Abstract

Structural failure of the accelerator grid in two-grid ion optics due to charge exchange ion erosion is considered one of the dominant failure modes for ion engines. A detailed examination of three accelerator grids used in long duration tests of inert gas ion thrusters was undertaken to characterize the radial mass loss distribution, the local distribution of mass loss in the erosion pattern and how it varies as the pattern evolves. The results show significant broadening of the radial profile compared to what is expected in space with significant variations from grid to grid. The local distribution of mass loss and how it varies with increasing total mass loss in the erosion pattern was also found to differ considerably among the three grids. The results indicate that the details of the erosion geometry cannot be ignored when generalizing test results or modeling grid failure to calculate useful engine service life,

Introduction

Xenon ion propulsion offers a number of benefits for Earth-orbital and planetary mission applications. Because of its high efficiency and specific impulse capability, ion propulsion can significantly decrease the propellant mass or deliver more payload mass and, for many planetary missions, substantially decrease the trip time. Because ion engines are inherently low

thrust devices, however, extremely long burn times are required. For instance, a typical small body rendezvous mission would require an engine service life of 8000-12000 hours. Demonstrating engine reliability for such a long service life by testing alone would be prohibitively expensive, so lifetime assessment for engine wearout failure modes must rely to a large extent on analysis based on an understanding of the physics of failure. One of the dominant failure modes for inert gas ion engines with two-grid optics is thought to be structural failure of the downstream grid due to ion sputter erosion. Although the magnitude of the grid wear is dependent on the grid material, the operating conditions and the engine environment, the process is inherent in ion engine operation and cannot be avoided. To better understand the spatial distribution and temporal variation of accelerator grid erosion, an analysis of the erosion patterns on three grids used in long duration tests of 30 cm ion engines was combined with models of the physical processes involved in grid wear. The results show that the useful engine life is strongly dependent on the local and global distribution of erosion and that the distribution changes with operating time.

Accelerator Grid Erosion Phenomena

A diagram of the electrode system in a two-grid ion thruster is shown in Fig. (1). Discharge ions produced upstream are drawn through a sheath that forms at the entrance to the apertures in the screen grid and are accelerated by an axial electric field in the inter-electrode gap. A radial electric field in this region focusses the individual ion beamlets. The accelerator (accel) grid is biased negative relative to the ambi-

* Technical Group Leader

† Group Supervisor

‡ Member of the Technical Staff

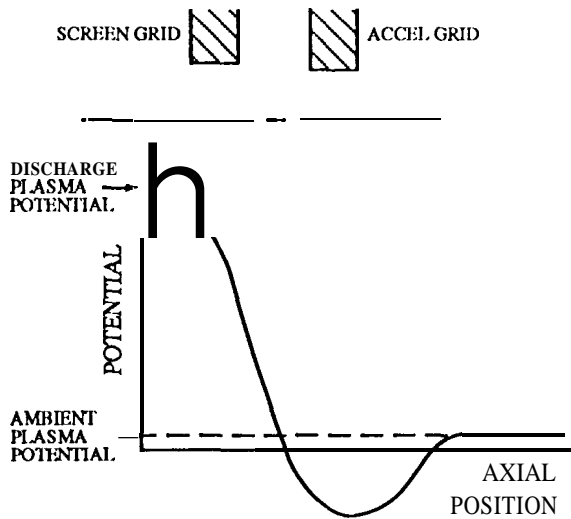


Figure 1: Diagram of two-grid electrode system and axial potential distribution.

ent space plasma potential to prevent electrons that neutralize the primary ion beam downstream of the engine from **backstreaming** into the discharge chamber. This creates a negative potential well which decelerates the primary ion beamlets. The beamlets are also subject to radial electric fields in this region which cause them to diverge.

The accel grid may be impacted directly by primary beam ions, although this source of impingement current can be practically eliminated by proper design and operation of the ion optics. In addition, the accel grid collects slow ions generated from neutral gas in the interelectrode gap and downstream of the grid. In space, the engine is the only source of neutral gas. An inevitable consequence of propellant utilization inefficiencies is the leakage of neutral atoms from the discharge chamber, although the density of these source atoms drops rapidly downstream of the grid [1]. In ground test facilities a second population of ambient gas atoms can exist with a more or less uniform distribution and a density determined by the engine propellant flow rate and the pumping capability of the facility.

These neutrals can be ionized either by collisions with electrons produced by the neutralizer cathode or in charge-exchange collisions with primary beam ions. In charge exchange collisions a thermal neutral atom surrenders an electron which recombines with a high speed ion. This creates a high velocity neutral atom that escapes with the beam and a thermal ion. Order of magnitude analyses and experiments indicate that the contribution from electron-impact ionization is small compared to that from charge exchange processes [1].

The majority of charge exchange ions created in the deceleration zone downstream of the accel grid do not have sufficient energy to escape from the potential well and are therefore drawn to the accel grid. Experiments and particle simulations indicate the existence of a slight potential hump downstream of the deceleration zone in the beamlets. In contrast, the potential appears to decrease monotonically toward the accel grid between adjacent beamlets [1, 2]. Therefore, a fraction of the slow ions generated in the weak electric field downstream of the neutralization plane can be collected if their velocity is back toward the grid when they are created. In space, most of the neutrals emitted from the discharge chamber have velocities directed away from the grids, so very few of the charge exchange ions created downstream of the deceleration zone will be collected [3]. In addition, the density decreases rapidly in the axial direction, so fewer ions are generated downstream. However, in ground test facilities the ambient neutrals have an isotropic velocity distribution and a significant quantity of the ions created downstream will impinge on the accel grid. In fact, the charge exchange ions generated from the background gas appear to dominate the impingement current in ground-based tests [3, 1].

The impingement ions follow trajectories that are dictated by their origin and the structure of the potential near the grid. Particle simulations show that most of the ions impinge on the downstream face of the electrode and are focussed into the central part of the webbing between holes by the radial electric fields of adjacent beamlets [2, 4]. The characteristic erosion pattern observed on the downstream face of the accel grid in long duration tests reveals the damage caused by the impingement ions. The photograph in Fig. (2), taken after a long duration test described in [5], shows a series of grooves between apertures

forming a hexagonal pattern with deeper pits at the intersection points between three holes where the impingement current density peaks.

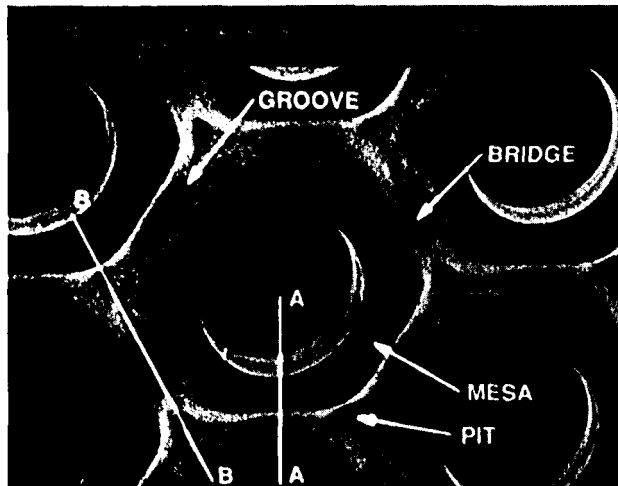


Figure 2: Photograph showing the characteristic form of accel grid erosion on the downstream surface.

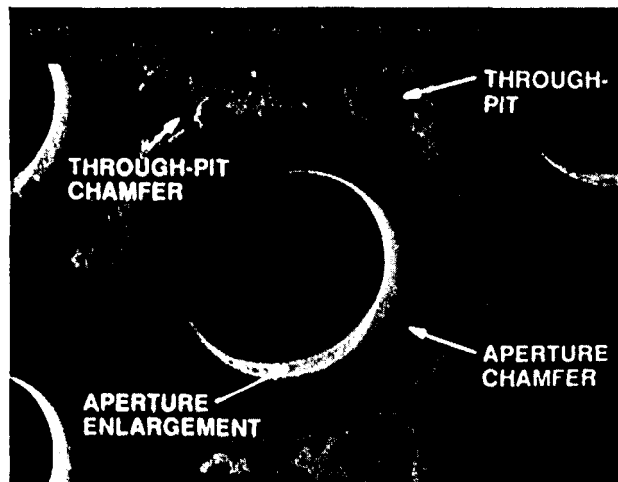


Figure 3: Photograph showing the erosion structures typically found on the upstream surface.

The mass loss in the pits and grooves is caused by sputtering, a collisional process in which incident ions can eject surface atoms. Sputtering occurs only when the incident ion energy exceeds a certain threshold and sufficient energy is transferred in the collision to overcome the surface binding forces. At energies near the threshold the ejected atoms are usually directly

involved in collisions with the incident ion, although at higher energies they may be part of a collision cascade initiated by the incident ion. Sputtering is characterized by the yield, which is defined as the expected number of atoms ejected per incident ion. The yield is a function of the ion energy, the masses of the ions and target atoms, the surface binding energy and the incident angle, reaching a maximum value at a particular oblique angle. It does not generally depend on the current density, but is a function of the total dose. This can be due to radiation damage accumulation in the target lattice, but in accel grid erosion is primarily due to changes in the geometry due to wear. Initially the impingement ions are normally incident on a flat surface, and most of the sputtered atoms escape. As the grooves form, the incident angle may increase, causing the absolute yield to rise. However, redeposition of sputtered atoms in the groove can actually result in a decrease in the net yield [6]. As the pits and grooves penetrate the accel grid, the net yield may once again increase as sputtered atoms escape upstream through the grid.

When the pits wear completely through the grid, the ions incident in that region are either reflected in the interelectrode gap and strike the upstream face or are focussed along the channels. The upstream surface of the grid in Fig. (2) is displayed in Fig. (3) and shows six triangular through-pits surrounding one aperture and chamfering around each through-put caused by ions reflected in the gap. In addition, erosion of the aperture walls and upstream edge by direct ion impingement or charge-exchange ions created in the interelectrode gap is noted. After the through-pits form, grid penetration proceeds along the channels until complete structural failure occurs. Loss of grid structural integrity as a result of sputter erosion in the characteristic hexagonal groove pattern is one potential failure mechanism. Loss of strength caused by grid erosion can cause shorts as individual ringlets or sections of the accel grid collapse and bridge the interelectrode gap under the electrostatic stresses. Even if shorts are avoided, it becomes impossible to properly focus the primary ions and prevent electron backstreaming as large holes in the grid form.

Accelerator grid sputter erosion can be minimized by proper environmental conditions and thruster operation, but is unavoidable at some level. Relying

on extensive testing to characterize the grid failure probability would be prohibitively costly and time-consuming. It is therefore necessary to model accelerator grid erosion, using available test data and knowledge of the physical processes that lead to failure.

Models of Accelerator Grid Failure

Models of the time to structural failure of the accel grid can be grouped in two classes: models which predict the integrated mass loss over the entire grid as a function of time and use a total mass loss to define the end-of-life and models which predict the local erosion rate in the grid center where structural failure first occurs and use a local eroded depth or local mass loss as the end-of-life criterion. An example of the first model type was presented in [7], in which the total grid mass loss M_e per unit dose of impinging ions, defined as the product of the impingement current J_a and the operating time t , is correlated with the accel grid voltage measured in five long duration tests. A linear regression relating the mass loss parameter to the grid voltage is used with a total acceptable mass loss of 70 g, based on the successful completion of a test in which 85 g of material were lost [5], to determine the useful grid life for a given impingement current and grid voltage. This approach has the advantage of relating the grid life to macroscopic engine parameters, but the failure criterion is arbitrary and it is not clear that conservatism is preserved when the geometry of erosion and the variation of the erosion distribution in time is ignored.

It is generally agreed that structural failure will occur first in the grid center when the bridges between erosion pits are completely worn away, leaving the ringlet surrounding a single aperture free. Models of failure in the grid center can be further divided into two categories, those that correlate local erosion rates with global engine parameters and those that consider the global and local distribution of mass loss. The simplest model of local grid failure outlined in [8] is based on the assumption that the erosion rate in the bridge region is constant. An average eroded depth of 76 μm at the bridges in the center of a 30 cm diameter grid measured after 906 hours of operation on xenon at 5.5 kWc was used to calculate a bridge erosion rate of 84 $\mu\text{m}/\text{hr}$. Extrapolating this erosion rate to failure yielded a lifetime at the ground

test conditions of 4300 hours and a total mass loss of 77 g. This rate was then scaled by the ratio of the impingement current expected in space to that measured in the test to yield a useful life of over 11,500 hours in space. This rate could also be scaled by the ratio of sputter yields at different energies corresponding to accel grid voltages to predict the time to failure for different operating conditions, assuming that all of the impinging ions strike the surface with the full grid potential,

$$\dot{d}_{b2} = \left(\frac{d_{b1}}{t_1} \right) \left(\frac{J_{a2}}{J_{a1}} \right) \left(\frac{Y_2}{Y_1} \right) \quad (1)$$

In this equation \dot{d}_{b2} , J_{a2} and Y_2 are the bridge erosion rate, accel grid impingement current and sputter yield for condition 2, and d_{b1} is the bridge eroded depth observed in time t_1 and J_{a1} and Y_1 are the corresponding impingement current and yield. This model is also simple to use, but relies on an extrapolation to operating times over an order of magnitude longer than actual test experience using an unsubstantiated assumption of a constant erosion rate.

To study the geometry of the grid erosion and the approach to structural collapse a two grid, 30 cm ion accelerator system was tested to failure [9]. The wear rate was artificially accelerated by operating at a vacuum chamber pressure of 3.5×10^{-3} Pa and a comparatively high accel grid voltage of -500 V. The engine actually failed after 633 hours when the grids were shorted together by a flake of material that had been sputter-deposited on the screen grid from the accel grid, but the grid was also very near structural failure. Inspection of the grid after 145 hours and 633 hours showed that the erosion was largely confined to the pits and grooves pattern and that the fraction of the webbing area encompassed by this pattern (determined by the diameter of the pits and the width of the grooves) was approximately constant with radial position on the grid and over the course of the test. These observations led to the definition of a failure criterion based on the removal of all of the material in the pits and grooves pattern in the center of the accel grid where the impingement current density is highest, with the assumption that the grooves are square channels with straight, vertical walls. The total mass loss at failure is then given by the expression

$$M_f = A_b t_a \rho (1 - \phi_a) \alpha f_a, \quad (2)$$

parabolic cross-section. This reflects the experimental observation that the cross-section in the bridge region is approximately parabolic when the bridge is finally penetrated in the center while the cross-section in the pits at failure is much closer to square. The failure criterion is defined as the point at which sufficient mass has been removed from the erosion pattern with the chosen cross-sectional area that the bridges surrounding the center hole collapse.

The model was used to assess the service life capability of the 30 cm diameter xenon ion engine proposed for the NSTAR (NASA SEP [Solar Electric Repulsion] Technology Applications Readiness) Program. At a power level of 4.65 kWe and with an eroded area fraction of 0.4 the useful service life of the engine with a 50% risk of failure (corresponding to the deterministic life estimate using nominal values of the input parameters) was only 4070 hours and the life with 0.1% failure risk was 2100 hours. At a derated power level of 2.3 kWe the corresponding lifetimes were about five times higher. This shows that the lifetime with acceptable failure risk can be substantially lower than that estimated deterministically using nominal parameter values. Uncertainties about the eroded geometry at failure, the net sputter yield and the impingement ion current in space were found to be the primary risk drivers.

This approach accounts for the geometry of the erosion pattern, but only predicts the point of failure. It cannot be used to describe the local geometry prior to failure, so it is difficult to compare it with non-failure test data.

Another approach based on an empirical correlation of the local erosion rate to global engine parameters is discussed in [11]. This correlation, plotted in Fig. (4), relates the average eroded bridge depth in the grid center to a "Grid Erosion Parameter" (GEP) defined as

$$GEP = \frac{J_a \gamma t}{A_b}. \quad (6)$$

Data from seven long duration tests are fit with a line, implying a relationship of the form

$$d_b = C_0 + C_1(GEP) \quad (7)$$

where d_b is the average eroded depth at the bridges in the grid center and C_0 and C_1 are constants. Extrapolating this correlation to the point of grid structural failure yields unreasonably long lifetimes, so its use

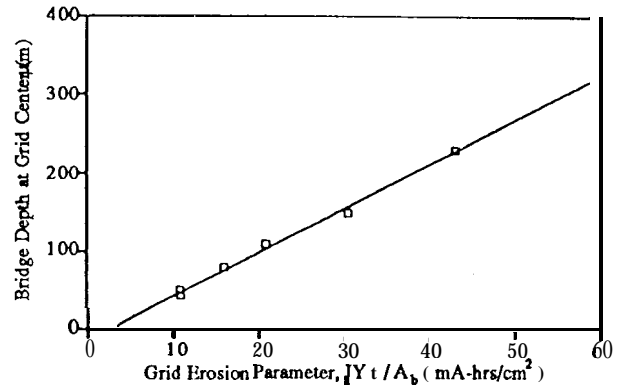


Figure 4: Correlation between the eroded bridge depth and global thruster parameters.

has been restricted to values of the GEP less than 40, for which it generally predicts service life values much larger than the models based on total or local mass loss in the pits and grooves pattern. No physical justification for a linear relationship between the local erosion rate in the grid center and these global parameters has been proposed, and it is not clear that ignoring the local erosion geometry is justified.

The measurements discussed in this paper were made to characterize the spatial distribution of mass loss and the variation in erosion rates with ion dose to gain a better understanding of the local erosion processes. The objective was to test the assumptions of the various models; in particular to resolve whether the details of the spatial and temporal distribution of mass loss can be ignored in correlations relating a particular failure criterion to global engine operating parameters.

Analysis of Grid Erosion Structures

Grid Documentation and Wear Test Conditions

The global and local distribution of mass loss on three 30 cm diameter accelerator grids from two-grid optics systems used in long duration tests with inert gas propellants were studied using several different techniques. The three grids were designated Grid 42, Grid X901 and the TTF Grid. The grid geometry

Grid	Measured Thickness (mm)	hole Diameter (mm)	Center-Center Hole Spacing (mm)	Open Area Fraction	Dish Depth (cm)	Dish Diameter (cm)	Active Area Diameter (cm)	Refs.
42	0.564	1.27	2.21	0.30	2.34	30.5	28.6	[5, 7]
X901	0.373	1.14	2.21	0.24	2.5	31.4	28.6	[8]
TTFT	0.361	1.14	2.21	0.24	2.1	28.9	28.6	[9]

Table 1: Accelerator grid geometry.

Grid	Thruster	Propellant	Tank Pressure (Pa)	Accel Volt age (v)	Beam Current (A)	Accel Current (mA)	Test Duration (Hours)	Refs.
42	J2	Hg		-300		4	520	[5, 7]
		xc		-500		25	300	[5, 7]
		Xe	2×10^{-3}	-510	5.0	47	740	[5, 7]
X901	Lab Model	Xe	1.7×10^{-3}	-330	3.2	17.4	1160	[8]
TTFT	J-Series	xc, Hg						
		Xe	$3.5-4 \times 10^{-3}$	-500	2.8	35	633	[9]

Table 2: Wear Test Conditions.

and a summary of the test histories are given in Tables (1) and (2). Further details can be found in the indicated references. Grid 42 is a J-series accel grid with a substantial previous test history. The final test described in [5, 7] was with a J2 thruster operated on xenon at 10 kWc for 740 hours. Before this test the grid had deep pits and grooves with small through-pits out to a radius of 5 to 7.6 cm, Grid X901 is a modified J-series grid with a deeper dish depth and dish radius which was run on xenon with a laboratory model ring-cusp thruster at 5 kWc for 1160 hours [8]. The grid had not been used prior to this test. The TTFT Grid is a J-series accel grid used in the test-to-failure discussed above [9]. The engine was a J-series thruster which had been modified to operate on inert gases and approximate the magnetic field configuration of a ring-cusp engine. The grid had been used in an undocumented amount of previous testing, but there was minimal erosion prior to the final test.

Grid Erosion Measurement Techniques

Two types of analyses were conducted on these grids; a measurement of the radial mass loss profile and characterization of the scale and distribution of erosion on the surface. The radial mass loss distribution was measured by cutting the grids into seven

concentric rings by wire electro-discharge machining (EDM). The first cut produced a disk with a diameter of 1.27 cm. Subsequent cuts were made in radial increments of 2.54 cm. The width of the cut using this process is only about 0.3 mm. The rings were then weighed, in general using two balances with the better balance providing a resolution of less than ± 2 mg. Agreement between the two measurements was invariably excellent. The actual inner and outer diameter of the rings were measured and used to calculate the ring surface area, correcting for the grid curvature. These measurements yielded the final mass per unit area for each ring, which was subtracted from an estimate of the initial mass per unit area to obtain the mass loss per unit area. The initial mass was estimated using the relationship

$$M_i'' = (1 - \phi_a)t_a\rho, \quad (8)$$

which is the largest source of potential errors. The grid thickness t_a , listed in Table (1), is the thickness calculated from measurements made on the periphery where no erosion is expected with a correction which assumes a uniform thinning of the grid in the dish region from the hydroforming process. The calculated thickness has an uncertainty on the order of $\pm 5\%$. The density of the TTFT grid was measured and found to be within 2% of the published density of

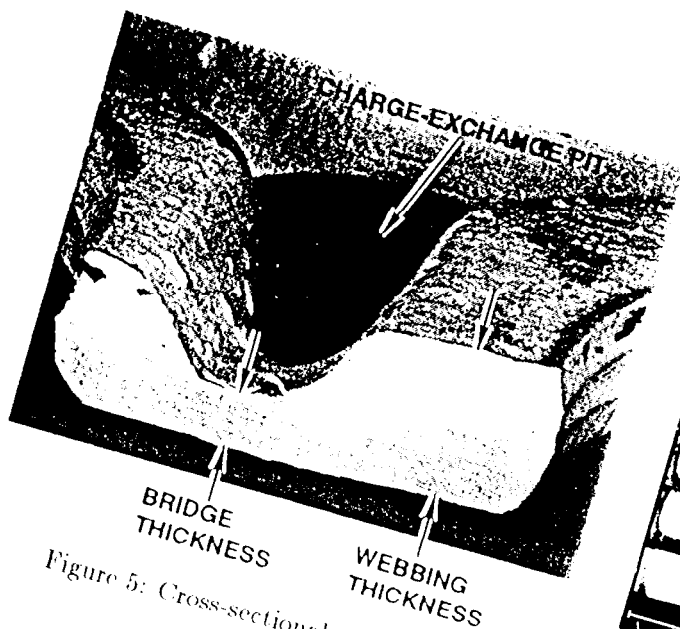


Figure 5: Cross-sectional cut along A-A.

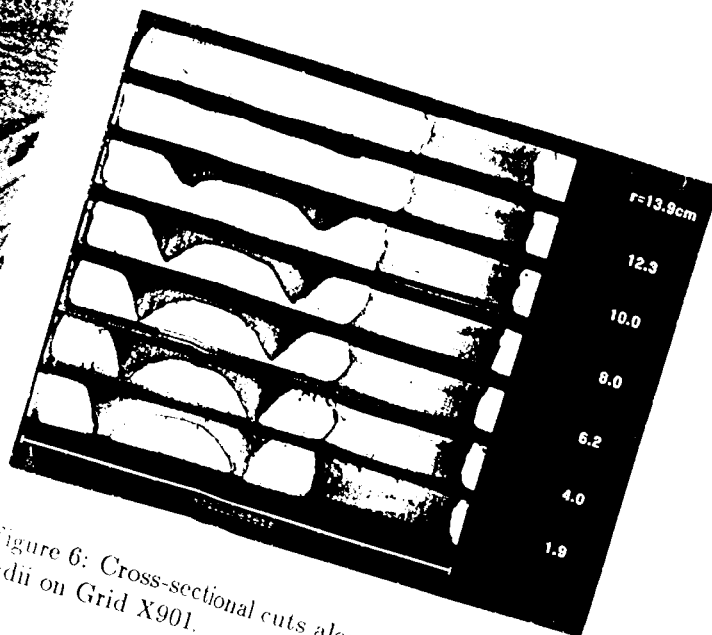


Figure 6: Cross-sectional cuts along B-B for different radii on Grid X901.

10.22 g/cm² for molybdenum. The term correcting for the open area fraction does not account for details of the geometry such as the etch cusps in the apertures, and may therefore introduce additional small errors. The uncertainty in the mass loss per unit area is on the order of $\pm 4.5\%$.

Two methods were used to measure the scale of erosion damage on the grid; profilometry and direct measurements on sectioned pieces of the rings in a scanning electron microscope (SEM). A Cyberoptics PRS-40 laser profilometer was used to characterize Grids 42 and X901. This unit has a vertical range of 400 μm with a resolution of 1 μm and a lateral scan positioning accuracy of about 0.5 μm . Scans along webbing cross-sections A-A and B-B indicated in Fig. (2) were performed for each hole along a single radius of each grid. The scans were made normal to the thrust axis, not the local surface normal, so the profiles had to be leveled digitally to correct for the grid curvature. The largest source of error in these measurements was associated with alignment along the proper scan trajectory. The endpoints of each scan were set manually by observing the laser spot on a magnified image of the grid, so small deviations from paths A-A and B-B were possible. However, examination of the grid topology in the areas of interest suggests that the important measurements are not particularly sensitive to misalignment.

After the profilometry and mass loss analysis were completed small sections were cut from each of the rings using EDM or a diamond saw. The edges of these grid bits were then polished to provide smooth radial cross-sections along cuts A-A and B-B. Figure (5) shows an image of one of the cuts along section A-A which extends along a bridge connecting the two ringlets surrounding adjacent holes. Examples of the surfaces corresponding to section B-B are shown in Figures (6)-(8). The white areas are the polished surfaces which contain two pits and cuts across the bridge connecting the two holes normal to the image. On either side of the polished section are the walls of the two apertures that lie in the plane of the image. Dimensions were measured using cursors that could be placed directly on the image in the SEM monitor with an uncertainty of about 1% of the image size or using cursors on images stored to disk, although these measurements were limited in resolution by the size of the pixels, which were 3-6 μm square. The largest errors were again associated with alignment of the cuts of proper endpoints on the image to characterize the sectional area of the bridges was calculated from images like those in Figures (6)-(8) using image analysis software. Uncertainties in these measurements were

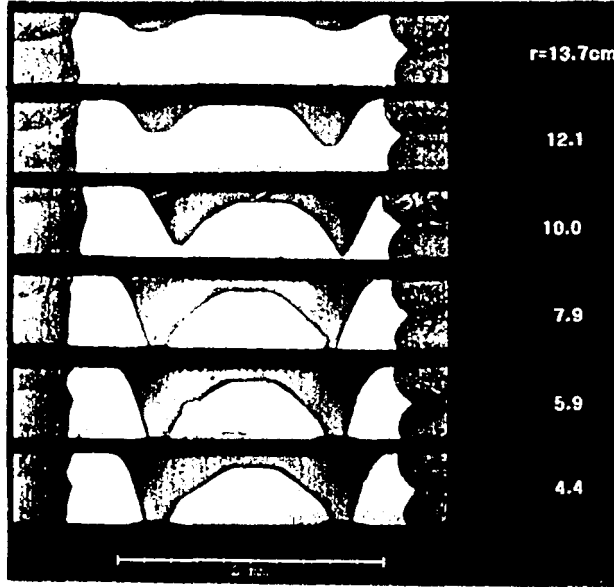


Figure 7: Cross-sectional cuts along B-B for different radii on Grid 42.

due primarily to inhomogeneities in the cross-section image, but were probably less than about $\pm 3\%$.

Results and Discussion

Macroscopic Broadening of the Erosion Profile

The mass loss per unit area is displayed in Fig. (9) and a summary of the integral and distribution characteristics is given in Table (3). The integrated mass loss agrees well with that calculated for Grid 41 [7] and the measured value for Grid X901. The TTTT Grid lost about **44 g** of material in the final test, so the 18 g difference between that and the integrated value was probably lost in prior tests,

The erosion profile flatness parameter, defined as the ratio of the average mass loss per unit area to the peak value, demonstrates how different the profiles for the three grids are. This is shown dramatically in the plot of fraction of enclosed mass loss as a function of radius in Fig. (10). This figure shows, for instance, that 50% of the total mass loss from Grid 42 occurred from within a radius of 9.6 cm, and was distributed

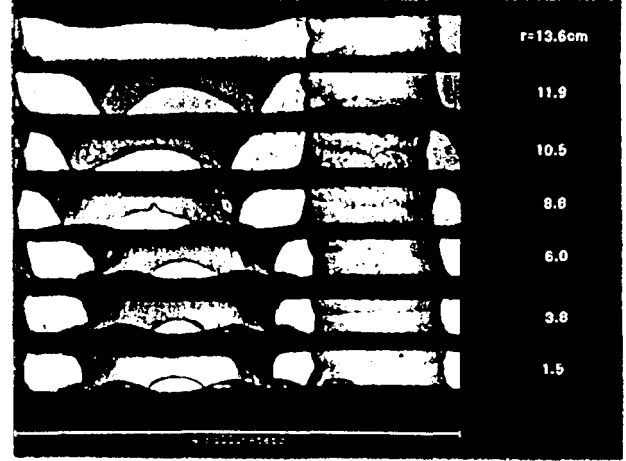


Figure 8: Cross-sectional cuts along B-B for different radii on the TTTT Grid.

over an area of 292 cm^2 . In contrast, 50% of the mass loss from Grid X901 was contained within a radius of 7.9 cm, which contains only $2/3$ the area over which the same fraction of mass loss was distributed on Grid 42. The erosion profiles are also much broader than has been assumed for operation in space [10, 9]. The charge exchange ion formation rate at a particular point is given by

$$\dot{n}_{cx} = \frac{j_b}{e} n_0 \sigma_{cx} \quad (9)$$

where j_b is the beam current density, n_0 is the neutral density and σ_{cx} is the cross section for charge exchange reactions. In space the only source of neutrals is the engine and the density drops rapidly in the axial direction. Most charge exchange ions created from the neutral component of the plume will therefore be formed near the grids where the potential is dominated by the sheath and the equipotential lines are essentially parallel to the surface. These charge exchange ions will consequently strike the grid close to the same radial and azimuthal position where they were generated. The impingement current radial distribution should be controlled by the beam current density distribution and the radial distribution of the neutrals, both of which are peaked on the centerline. Ion engine beam flatness parameters are generally on the order of 0.5, which is significantly lower

Grid	Measured Mass Loss (g)	Integrated Mass Loss (g)	Average Loss/Area (mg/cm ²)	Peak Loss/Area (mg/cm ²)	Flatness Parameter f_a
42	85	85.3	137.9	154.6	0.89
TTFT		62.6	100.5	141.1	0.71
X901	19.8	21.3	34.7	56.6	0.61

Table 3: Grid Mass Loss Summary,

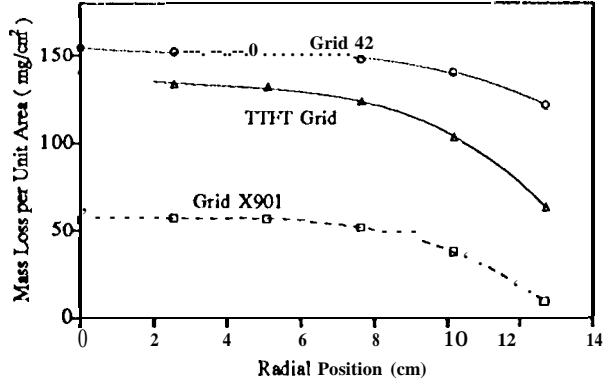


Figure 9: Radial distribution of mass loss per unit area.

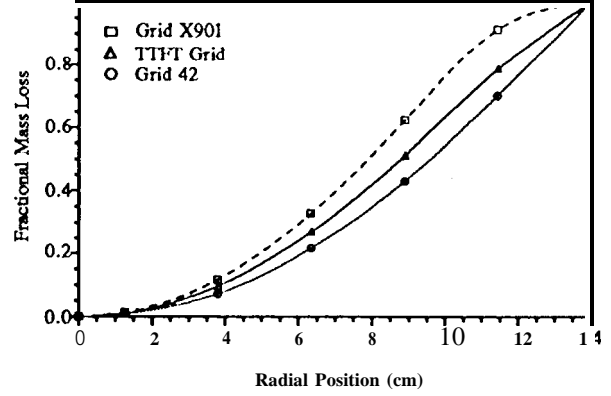


Figure 10: Fraction of enclosed mass loss as a function of radius.

than the flatness parameters for the erosion distributions, which range from 0.61 to 0.89. The broadening of the erosion profile is thought to be a ground test effect created by the generation of additional charge exchange ions far downstream from the ambient neutral gas present in test facilities. There are two potential mechanisms for this broadening. In a field-free beam the charge exchange ion trajectories will be determined by the distribution of thermal velocities. For an isotropic distribution, a charge exchange ion created on the centerline will have a much greater chance of hitting the grid at larger radii simply because the solid angle is larger for such impacts. In addition, a plasma plume expanding into a vacuum generates an ambipolar electric field which is perpendicular to the density gradient. Charge exchange ions created downstream in the plume will therefore be subject to a field with a radial component which tends to spread the distribution as it flows back toward the grid.

This hypothesis was qualitatively verified with a Particle-In-Cell (PIC) simulation of an ion plume interacting with two populations of neutrals, a neu-

tral plume from the engine modeled as free molecular flow from a point source and an ambient neutral gas with a uniform density. The computational details of the model are summarized in Appendix A and in [12]. This code was used to calculate the radial distribution of the impingement current generated by a beam with a gaussian current density profile. Figure (11) shows the beam current density, the impingement current density generated in the neutral plume from the engine, the accel grid current density from a uniform background gas and the total accel current density distribution, all normalized to the peak value of the distribution.

The accel current density distribution is close to the beam current distribution. Some broadening is apparent, evidently from charge exchange ions generated downstream of the sheath. The distribution from the uniform background neutrals is much flatter, though. As shown in this example, the total current density falls between the two profiles, but where it falls, the extent of the broadening, is determined by how much the ambient background gas dominates

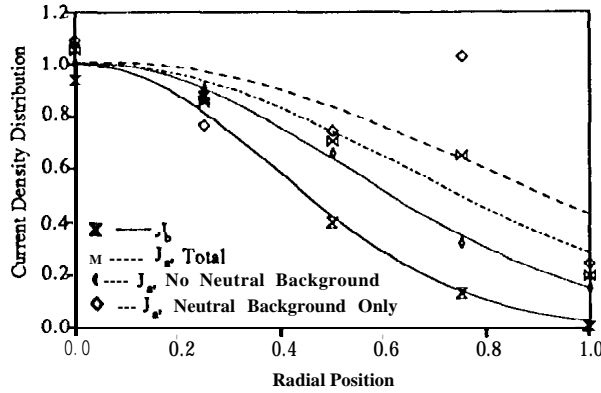


Figure 11: Distribution of beam and impingement current density from PIC simulation.

the charge exchange process.

Local Distribution of Erosion

As the photographs in Figures (2) and (3) show, the mass loss is also nonuniformly distributed locally on the grid. These erosion patterns were first characterized for these three grids by Rawlin [7] and Brophy [9]. More detailed examinations were conducted using the profilometer and destructive analyses to study the local distribution of erosion and determine how it changes with time. The mass loss sites indicated in Figures (2) and (3) were cataloged by Rawlin and include mesa erosion, aperture wall erosion, a slight chamfering of the upstream edge of the apertures, erosion in the pits and grooves pattern, and undercutting on the upstream edge of through-pits. Erosion of trenches around the periphery of the active beam area was observed in several tests, most notably the test-to-failure, and is discussed by Rawlin and Brophy. The excessive erosion on the grid periphery in the test-to-failure is suspected to be primarily an artifact of the high tank pressure used to accelerate the grid wear. Although this assumption has not yet been verified, that was not the focus of this analysis and the trench erosion was not examined.

Mesa erosion on the three grids was determined by measuring the web thickness in cross-sections along A-A or B-B next to apertures in the SEM, as shown in Fig. (5). The results for the three grids are plotted

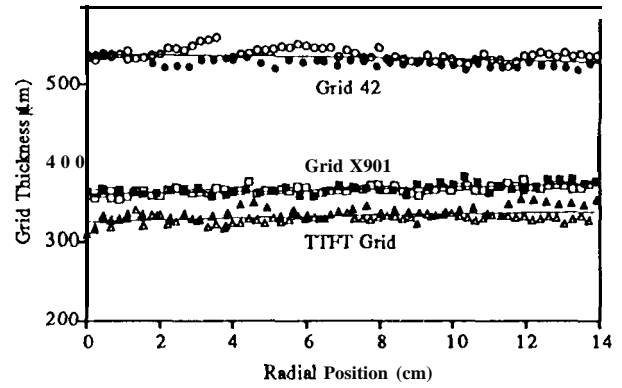


Figure 12: Grid webbing thickness as a function of radius.

as a function of radius in Fig. (12). The scatter in the data is larger than the uncertainty in the measurements and represents a real variation in webbing thickness from hole-to-hole. In addition, each curve is composed of six or seven segments, each of which comprises the measurements made on an individual grid bit. The grid bits from a particular grid were not necessarily taken from the same azimuthal location, so some of the scatter may be due to azimuthal asymmetries. The solid symbols are data taken from B-B cross-sections while the open symbols come from A-A cuts. Linear or quadratic functions were fit to the webbing thickness data and subtracted from the initial grid thickness listed in Table (1) to determine the depth of mesa erosion. Grid 42 appears to have lost only 28-35 μm of material, which is considerably less than reported in [7]. Grid X901 lost less than 10 μm and the test-to-failure resulted in the loss of 25-35 μm from the accel grid. The eroded depth was then converted to a mass loss per unit area (based on the entire grid area, as in Fig. (9)), which is plotted in Fig. (13). This shows that the mesa erosion in all three cases accounts for less than 5-10% of the total mass loss per unit area. The SEM photos show what appears to be pristine material located between the upstream hole chamfers on the grids, so the grid thinning does occur by erosion on the mesas, probably as a result of a finite impingement current density of ions not focussed into the pits and grooves.

Hole wall erosion was measured by Rawlin on Grids

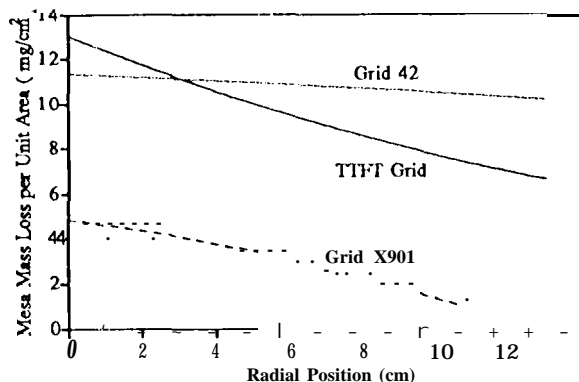


Figure 13: Mesa mass loss per unit area as a function of radius.

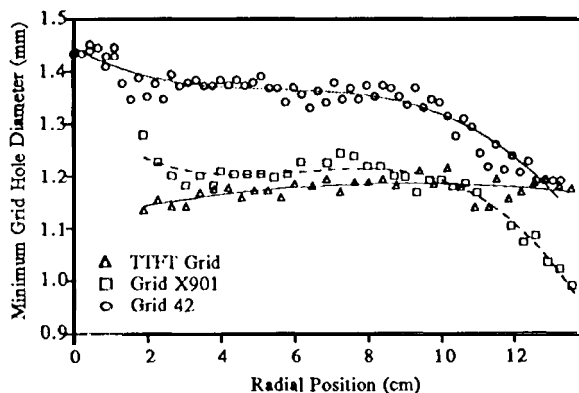


Figure 14: Minimum grid hole diameter as a function of radius.

X901 and 42" using precision pins [7]. The cross-sections obtained in this work complement these results by revealing more about how the hole walls wear. The minimum hole diameter was measured from SEM images and is plotted as a function of radius for the three grids in Fig. (14). The center hole diameter agrees well with the measurements by Rawlin, but the edge hole diameters are somewhat less than the nominal initial diameter. Photographs of the B-B cross-sections in Fig. (6) show the variation in the hole wall erosion with radius. In these images, the left hand side is the edge of one hole, the white portion is the webbing with two pits and a

bridge in the center and another aperture wall on the right hand side. The first image, of a site near the periphery, shows that both of the etch cusps are still visible. The hole diameter increases with decreasing radius and the wear is fairly symmetric azimuthally on the hole wall.

The measurements from Grid 42 agree well with the points measured by Rawlin. The photomicrographs in Fig. (7) show only the webbing in the B-B cut, but the aperture walls are visible on either side of the webbing. These photos show that the erosion is asymmetric--the cusp is essentially untouched on the right hand side, but is very worn on the left hand side. This is undoubtedly an effect of grid compensation or misalignment, in which the beamlets are closer to the innermost hole wall. The erosion occurs by direct ion impact or by the formation of charge exchange ions in the interelectrode gap or inside the aperture itself. These slow ions would be attracted to the hole wall closest to the beam.

The hole diameters on the TTFT Grid are quite uniform with radius and are about equal to the nominal pre-test value. The photos in Fig. (8) are similar to those from Grid 42, however, with asymmetric cusp erosion. This suggests that the pre-test diameter may actually have been slightly smaller than the nominal 1.14 mm.

The complete erosion of the cusps yields a mass loss per unit area which is on the order of 15 mg/cm^2 for Grid 42 and 6 mg/cm^2 for X901 and the TTFT Grid. The partial wear that is apparent in the photos represents only a few percent of the total mass loss per unit area, however. The photograph in Fig. (3) shows sputter-cleaning of an area around the hole on the upstream surface. This is another site which is subject to bombardment by charge exchange ions created in the interelectrode gap, but the erosion rates appear to be very low.

The models which account for the geometry of the erosion assume that essentially all of the mass loss is confined to the pits and grooves pattern. The pits and grooves were characterized by examining scans and cross-sections along cuts A-A and B-B in Fig. (2). A typical profilometer trace across a groove is shown in Fig. (15). This example shows that the groove cross-section can be reasonably well-represented by a parabolic profile, as assumed in the probabilistic model [10]. A profile along a groove shown in

steep walls, so the measurements are roughly equivalent to the width at the knees. This might cause an underestimate of the width for the probabilistic failure model because it assumes a profile with a shape that can vary from parabolic to square [10]

The TTFT Grid erosion structures were not measured with the profilometer, so SEM measurements of the width based on the knee locations are shown in Fig. (19). An estimate of the width of a parabolic

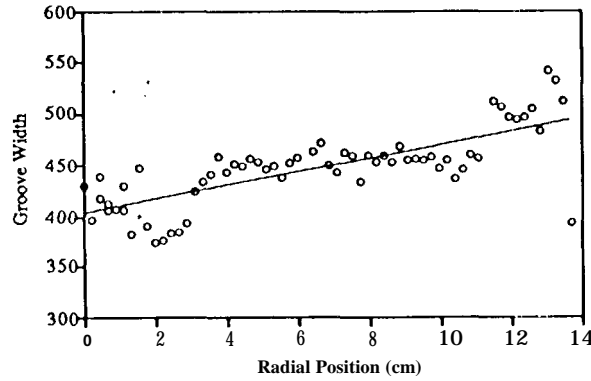


Figure 19: Groove width measurements for the TTFT Grid.

channel can be obtained by multiplying these values by 1.25. The groove width on the TTFT Grid also increases slightly with radius. The variation with radius is most likely due to decreasing beamlet current, which results in less focussing of the impingement ions. This interpretation is being investigated now with the 3DPIC code of a single aperture developed by ERC, Inc. [13, 3]

The measured groove widths were used to calculate the eroded area fractions shown in Fig. (20). These were calculated using widths based on the positions of the knees in the profiles and the parabolic fits to the data.

The models do not currently consider the distribution of mass loss within the pits and grooves pattern. The measured mass loss per unit area can be scaled into the area covered by the erosion pattern using the relationship

$$M_{pg}'' = \frac{M_{total}'' - M_{mesa}'' - M_{holes}''}{(1 - \phi_a)\alpha}, \quad (10)$$

where M_{total}'' is the aggregate mass loss per unit area

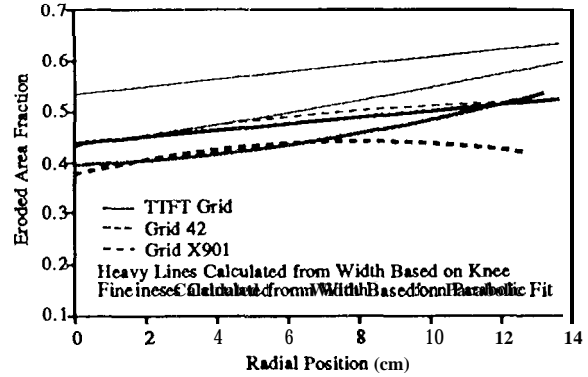


Figure 20: Eroded area fraction based on measured widths.

shown in Fig. (9), M_{mesa}'' is the mass loss per unit area due to grid thinning shown in Fig. (13) and the mass loss per unit area in the holes M_{holes}'' is considered negligible. When this value is multiplied by the local area covered by the pits and grooves pattern in the grid center, it yields the proper mass loss in that portion of the pattern. The mass loss per unit area in the pits and grooves is shown in Fig. (21) and can be related to an equivalent eroded depth d_{eq} if the erosion in this area were uniform,

$$d_{eq} = M_{pg}'' / \rho. \quad (11)$$

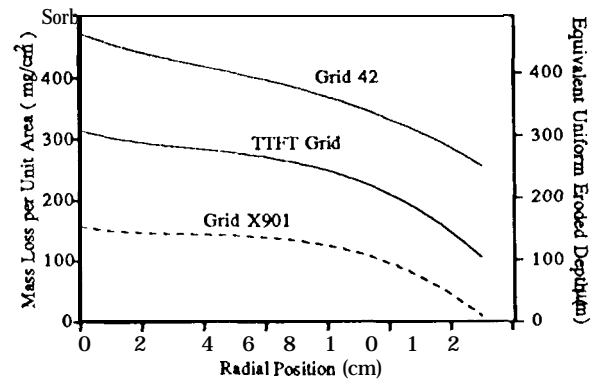


Figure 21: Mass loss per unit area scaled into the pits and grooves pattern.